Highly efficient BiOBr/red phosphorus heterojunction photocatalyst for Cr(Ⅵ) photoreduction (English)

QI Xian-Hui, ZHAO Hong-Gang, MA Yu-Hua, WANG Zhuan-Hu, LI Yun-Peng, LI Yu-Chen, LI Jia-Wen, YAN Chen-Xiang

DOI:10.11862/CJIC.2023.011
Chinese J. Inorg. Chem., **2023**,**39**(00):-

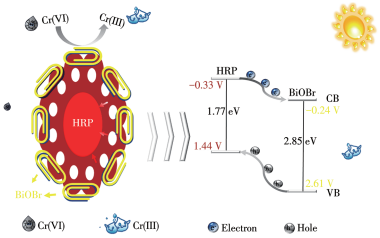

The BiOBr/HRP (HRP=hydrothermally treated red phosphorus) composite nano-photocatalyst were controllably fabricated by hydrothermal synthesis, and different photocatalytic activities were obtained depending on the BiOBr-to-HRP molar ratios. The 7%BiOBr/HRP photocatalyst can reduce almost all of the Cr(Ⅵ) completely within 20 min, and its excellent photocatalytic activity is attributed to the upgraded photoelectrochemical and charge carrier separation properties.

高效BiOBr/红磷异质结光催化剂用于Cr(Ⅵ)光还原

齐献慧[1] 赵红刚*,[1] 马玉花*,[1,2] 王转虎[1] 李云鹏[1] 李钰宸[1] 李佳文[1] 闫沉香[1]
([1]新疆师范大学化学化工学院,乌鲁木齐 830054)
([2]新疆师范大学,新疆储能与光电催化材料重点实验室,乌鲁木齐 830054)

摘要: 将水热处理后的红磷(HRP)与溴氧化铋(BiOBr)相结合,构建BiOBr/HRP异质结复合材料。通过调节和优化组成比例,7%BiOBr/HRP复合材料(复合材料中BiOBr的质量分数为7%)表现出最高的光催化活性,其可见光还原Cr(Ⅵ)的速率常数为0.188 min^{-1},是纯HRP(0.037 6 min^{-1})的5倍。在窄带隙HRP中引入宽带隙BiOBr所构建的异质结复合材料,扩大了可见光光谱吸收范围,增强了光的吸收,加速了光生电子和空穴的分离。

关键词: 红磷; BiOBr; 异质结; Cr(Ⅵ); 光催化
中图分类号: O643.36 **文献标识码:** A **文章编号:** 1001-4861(2023)00-0000-12
DOI: 10.11862/CJIC.2023.011

Highly efficient BiOBr/red phosphorus heterojunction photocatalyst for Cr(Ⅵ) photoreduction

QI Xian-Hui[1] ZHAO Hong-Gang*,[1] MA Yu-Hua*,[1,2] WANG Zhuan-Hu[1]
LI Yun-Peng[1] LI Yu-Chen[1] LI Jia-Wen[1] YAN Chen-Xiang[1]
([1]*College of Chemistry and Chemical Engineering, Xinjiang Normal University, Urumqi* 830054, *China*)
([2]*Xinjiang Key Laboratory of Energy Storage and Photoelectrocatalytic Materials, Xinjiang Normal University, Urumqi* 830054, *China*)

Abstract: Herein, hydrothermally treated red phosphorus (HRP) was combined with bismuth bromide oxide (BiOBr) to construct BiOBr/HRP heterostructure composite. Regulating and optimizing the composition ratio, 7%BiOBr/HRP (The mass fraction of BiOBr in the composite was 7%) exhibited the highest photocatalytic activity, the rate constant for visible light reduction of Cr(Ⅵ) was 0.188 min^{-1}, which was five times higher than that of pure HRP (0.037 6 min^{-1}). The heterojunction composite constructed by introducing wide band gap BiOBr into narrow band gap HRP expanded the visible spectral absorption range, enhanced the light absorption, and accelerated the separation of photo-generated electrons and holes.

Keywords: red phosphorus; BiOBr; heterojunctions; Cr(Ⅵ); photocatalysis

The current photocatalysts are faced with the problems of low solar light utilization and rapid electron-hole recombination, which limit the wide application in practice, so it is imperative to develop efficient semiconductor photocatalysts[1]. Among them, red phosphorus (RP) has been widely studied for its narrow band gap (1.4-2.0 eV), excellent response-ability to visible light, high stability, non-toxicity, abundant real estate, and low price[2-4]. However, due to the poor crystallization of amorphous RP, the easy recombination of photo-

收稿日期:2022-10-18。收修改稿日期:2022-12-07。
国家自然科学基金(No.52063028,22208275)、大学生创新创业训练项目(No.S202210762003,X202210762017,X202210762123)、新疆师范大学博士科研启动基金(No.XJNUBS1907)和新兴污染物与生物标志物监测创新团队(No.2021D14017)资助。
*通信联系人。E-mail:262385441@qq.com,15199141253@163.com

generated electrons and holes affect the practical application of RP in photocatalytic technology[5-6]. To improve this defect, the main strategies of modified RP are proposed, such as co-catalyst loading[7], immobilization[8], heterojunction[9]. Among them, the construction of heterojunction structures to accelerate carrier transfer and improve photocatalytic efficiency has become one of the most effective methods for RP modification. A large number of RP-based heterojunction composites have been reported, such as RP/TiO_2[10], RP/Bi_2O_3[11], RP/$Bi_2Fe_4O_9$[5], RP/$SrTiO_3$[12], RP/C_3N_4[9], RP/$BiPO_4$[13], and RP/Black phosphorus[14], and showed higher charge separation efficiency than a single material, thus greatly enhancing the photocatalytic performance of RP catalyst. Therefore, it is necessary to select a semiconductor that matches the energy band structure of RP and combine it to construct a more efficient heterojunction composite.

Bismuth oxyhalide (BiOX, where X=Cl, Br, I) exhibits significant photocatalytic properties under ultraviolet and visible light irradiation, and it has a tetragonal pyroxene structure containing a layer of $[Bi_2O_2]^{2+}$ plates interspersed by a double layer of halogen atoms. The lamellar structure therein provides a large enough space to polarize the relevant atoms and orbitals, and the induced dipoles can effectively separate the electron-hole pairs[11,14]. Among them, BiOBr with a band gap of 2.64-2.91 eV (visible light response)[15] and valence band composed of O2*p* and Bi6*s* hybrid orbitals[16], excellent photocarrier mobility and transport path[17-18], good chemical stability and environmental friendliness. It has been studied for wastewater treatment and is a very promising new photocatalytic semiconductor material[19-21]. The disadvantages of pure-phase BiOBr are mainly manifested in two aspects: Firstly, the absorption of visible light is relatively limited within a certain range, which leads to a relatively low light quantum yield; Secondly, the photo-generated electrons and holes are easily recombined, which leads to a further reduction in light quantum yield, seriously affecting the photocatalytic efficiency and limiting the development of its practical applications. Thus, the BiOBr semiconductor formed heterojunctions with other semiconductors, such as BiOBr/$BiPO_4$[22], BiOBr/$ZnFe_2O_4$[23], BiOBr/$CdWO_4$[24], BiOBr/WS_2[25], BiOBr/CdS[26], BiOBr/$NaBiO_3$[27], BiOBr/Bi_2MoO_6[28], and BiOBr/UMOFNs[20], which improved the charge transfer process and hindered the recombination of photogenerated carriers, thereby showing good photocatalytic activity.

Combined with the above analysis, the matching of the energy band structure between hydrothermally treated RP (HRP) and BiOBr helps to construct BiOBr/HRP heterojunction photocatalyst, its photoreduction ability was investigated by Cr(Ⅵ) reduction experiments under visible light irradiation. In addition, the reasons for the enhanced photocatalytic performance of the BiOBr/HRP heterostructure were investigated by serial characterizations.

1 Experimental

1.1 Preparation of BiOBr/HRP

Preparation of HRP: 0.6 g of commercial RP was dispersed in 20 mL deionized water, and hydrothermally treated at 200 ℃ for 12 h, then dried at 80 ℃ for 4 h, recorded as HRP.

Treatment of BiOBr: 0.000 5 mol·L^{-1} KBr of ethylene glycol solution was added drop by drop to the same concentration of $Bi(NO_3)_3·5H_2O$ of ethylene glycol solution, after stirring for 30 min to dissolve it completely, then moved into the reactor and reacted for 6 h at 160 ℃. After washing several times by using deionized water and anhydrous ethanol, BiOBr was obtained after drying overnight in a constant-temperature drying oven of 60 ℃.

Preparation of BiOBr/HRP (Fig. 1): BiOBr (Mass fraction of 5%, 7%, 9%, respectively) was mixed with HRP, the mixture was put into a hydrothermal kettle, and 20 mL deionized water was added. After reacting at 150 ℃ for 4 h, the mixture was washed and dried (80 ℃, 4 h) to prepare BiOBr/HRP. The catalysts were labeled as 5%BiOBr/HRP, 7%BiOBr/HRP, and 9%BiOBr/HRP, respectively.

1.2 Characterization

X-ray diffraction (XRD, D8 Advance) was used to analyze the phase composition of the catalyst by using

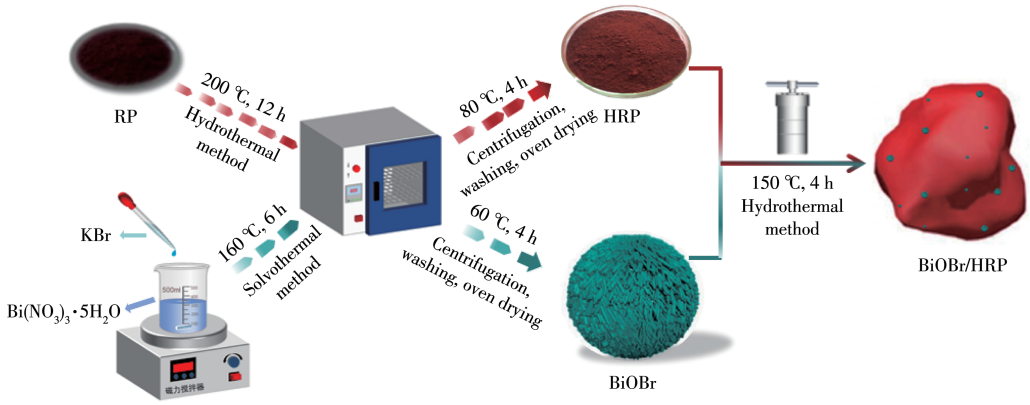

Fig.1　Preparation schematic diagram of BiOBr/HRP

the Cu $K\alpha$ radiation (λ=0.154 178 nm), tube voltage of 40 kV, tube current of 40 mA, scanning speed of 6 (°)·min^{-1}, and a 2θ range of 10°-70°. The particle size analyzer (Malvern, ZS90) was used to measure the particle diameter of the catalyst. The field emission scanning electron microscope (FESEM, Zeiss Sigma 500, operating voltage 5.0 kV) was used to investigate the morphology of the sample. The high-resolution transmission electron microscope (HRTEM, FEITecnaiF20, accelerated voltage of 50 and 300 kV) was used to inspect for the distribution and lattice analysis of sample nanoparticles. X-ray photoelectron spectroscopy (XPS) was used to observe the surface chemical element composition and valence states of the elements. UV-Vis diffuse reflectance spectrum (DRS, Pelambda750s) was used to investigate the optical absorption of samples. Photoluminescence spectrophotometer (PL, Fls920) was used to detect the PL spectra of samples. The electrochemical workstation (CHI660E) was used to test the electrochemical properties of the catalyst. The counter electrode was a Pt electrode, the reference electrode was an Ag/AgCl electrode, and the electrolyte was a 0.1 mol·L^{-1} Na_2SO_4 solution.

1.3　Photoreduction evaluation

$K_2Cr_2O_7$ and a 300 W xenon lamp were used as simulated Cr(Ⅵ) contaminant and light source, respectively. The detailed process was as follows: The composite photocatalyst (5 mg) was added into 20 mL 40 mg·L^{-1} $K_2Cr_2O_7$ solution. The mixture was magnetically stirred for 30 min in dark to reach the adsorption-desorption equilibrium and continuously stirred under light conditions for photocatalytic reduction. The supernatant (3 mL) was collected every 5 min through filtration by using a 0.45 μm filter. The supernatant was used to measure the absorbance of the solution at the maximum absorption wavelength of Cr(Ⅵ) (356 nm) to determine the remaining concentration.

2　Results and discussion

2.1　Characterization results

The XRD pattern was used to investigate the crystal phase and the structure of the prepared samples. The diffraction peak at 2θ=15° was the characteristic diffraction peak of the HRP amorphous structure (Fig.2a), which was well consistent with the literature reports[8,11]. The positions of the diffraction peaks at 2θ= 24.6°, 31.1°, 31.6°, 38.7°, 45.7°, 50.1°, 56.6° were in perfect agreement with the (101), (102), (110), (112), (200), (104), (212) crystal planes of the standard card of BiOBr (PDF No. 78-0348), respectively. No other impurity diffraction peaks appeared, which proved that the pure phase BiOBr had been successfully prepared and had high crystallinity and purity. For the 7%BiOBr/HRP composite, the diffraction peaks of the BiOBr and HRP were presented, and no other impurity phase was observed, indicating that the two semiconductors had been successfully combined.

The particle size of the sample was analyzed and shown in Fig.2b. The average particle size of 7%BiOBr/HRP was 122 nm, which was approximately one-third that of HRP (387 nm). The results further demonstrated that reasonable BiOBr can effectively control the parti-

cle size of the composite, and expand the specific surface area, thus increasing the active sites on the surface, which would contribute to the photocatalytic performance of HRP.

The microstructure and surface morphology of HRP, BiOBr, and 7%BiOBr/HRP nanoparticles can be visualized by SEM. It was observed that the uneven distribution of HRP particles resulted in an unsmooth surface, accompanied by a honeycomb-like void, showing a micropore structure (Fig.3a and 3b). This is due to a certain amount of phosphoric acid produced by RP under a certain temperature and pressure during the hydrothermal reaction, which had a secure etching effect on its surface[29]. The presence of this structure increased the specific surface area of RP and facilitated its full contact with pollutants, which had good adsorption and improved photocatalytic performance. The BiOBr had a relatively regular spherical shape

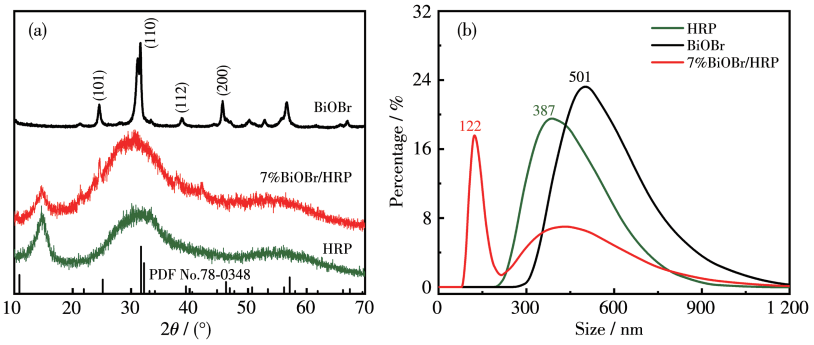

Fig.2 (a) XRD patterns and (b) particle size distributions of HRP, BiOBr, and 7%BiOBr/HRP

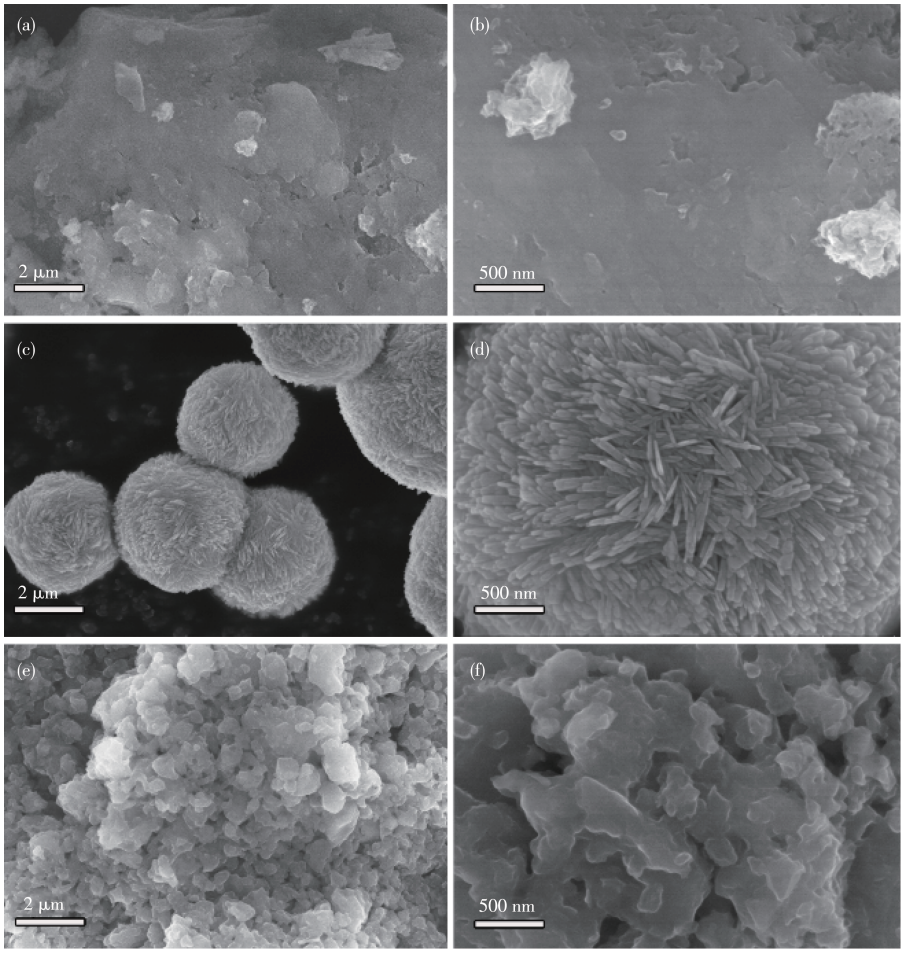

Fig.3 SEM images of (a, b) HRP, (c, d) BiOBr, and (e, f) 7%BiOBr/HRP

with a diameter of about 3 μm, the surface was interlaced with the nanoplates to form a flower-like microsphere structure (Fig.3c and 3d), which showed a better overall shape and more uniform distribution. Further magnification revealed that its structure was composed of elongated needle-like particles clustered at one end, one toward the center of the sphere and the other toward the outside of the sphere, forming a porous microsphere structure through self-accumulation. For 7%BiOBr/HRP, due to the strong interaction between the two interfaces, BiOBr adhered to the microporous fluffy HRP surface, taking the shape of a three-dimensional structure with intermediate porosity and diameter around 122 nm (Fig.3e and 3f). It showed regular aggregation and a relatively uniform porous structure with a diameter much smaller than that of HRP and BiOBr.

The morphology and crystal structure of the nanoparticles was observed by TEM. The HRP was dispersed by non-uniform particles and showed agglomeration (Fig.4a). The crystal structure was irregular, indicating that it was still amorphous after hydrothermal treatment (Fig.4b). Pure BiOBr showed a petal-like structure with nanoparticle sizes ranging from 235-640 nm (Fig.4c). The lattice stripes of BiOBr nanoparticles can be seen in the high-resolution magnification, the spacing of which was 0.23 and 0.28 nm (Fig.4d). Combined with XRD analysis, this value matched the (112) and (102) crystal planes of BiOBr, respectively. The BiOBr nanoparticles were uniformly distributed on the HRP surface (Fig.4e), and its high-resolution magnification can observe both the irregular crystal structure of HRP and the crystal plane of BiOBr (d=0.28 nm)[30], which confirmed that the BiOBr/HRP heterojunction photocatalyst had been successfully prepared. SEM and TEM results both disclosed that the HRP was immobilized on BiOBr to construct a decentralized porous structural composite, which expanded its specific surface area.

Further accurate analysis was obtanined by high-

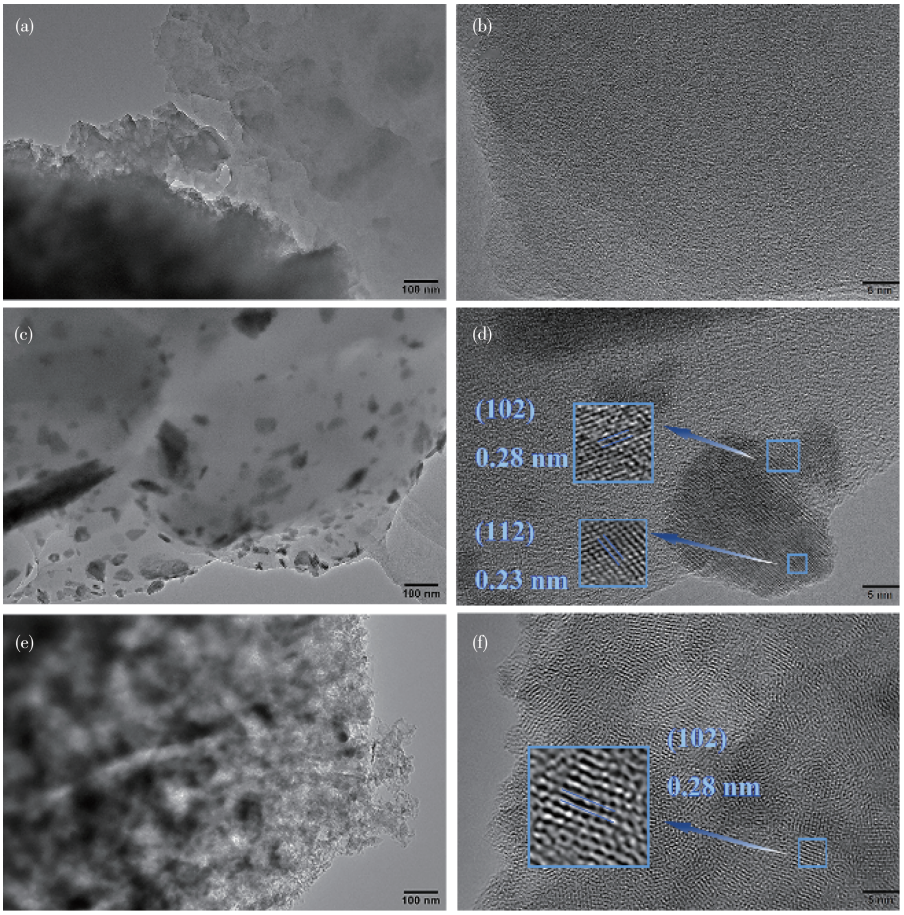

Fig.4　TEM images of (a, b) HRP, (c, d) BiOBr, and (e, f) 7%BiOBr/HRP

resolution XPS to element valence state and electron transfer. As shown in Fig. 5a, the two peaks at 159.2 and 164.5 eV correspond to the Bi4$f_{7/2}$ and Bi4$f_{5/2}$ of the trivalent oxidation state for Bi of pure BiOBr[31]. The splitting between these bands was 5.3 eV, referring to the presence of the normal state of BiOBr. In comparison to the pure BiOBr sample, the $Bi^{3+}4f_{7/2}$ peaks of 7%BiOBr/HRP exhibited a shift of about 0.4 eV toward lower binding energy, indicating that lower charged Bi ions were formed during recombination. The binding energy was reported to be influenced by the concentration of orbital electrons, which led to a slight shift of the peak[31]. And it appeared two new peaks at 162.4 and 163.8 eV, which may be due to the generation of Bi and Bi oxides (Fig.5a). The structural Br^- ions in the BiOBr surface exhibited a spectral doublet at 68.1 and 69.1 eV due to photoelectron emission from the 3$d_{5/2}$ and 3$d_{3/2}$ microstates[14] (Fig. 5b). In addition, the O1*s* peak can be divided into two peaks at 531.0 and 529.7 eV (Fig.5c). The peak at 529.7 eV was attributed to the lattice oxygen in BiOBr, while the other peak with a higher energy of 531.0 eV can be ascribed not only to the surface hydroxyl oxygen but also to the oxygen vacancies in the surface of BiOBr[32]. The P2*p* orbitals in HRP were located at 130.1 and 131.0 eV (Fig. 5d), which attributed to P2$p_{3/2}$ and P2$p_{1/2}$, while the peak appearing around 134.6 eV was a broad and weak peak, which was affiliated to the P—O bond[31]. On the contrary, the binding energies of the P2$p_{3/2}$ and P—O bond in 7%BiOBr/HRP were located at 130.2 and 134.8 eV, which were 0.1 and 0.2 eV higher than those in HRP, respectively. The above characterization results demonstrated that the interaction between BiOBr and HRP, heterojunction was constructed successfully.

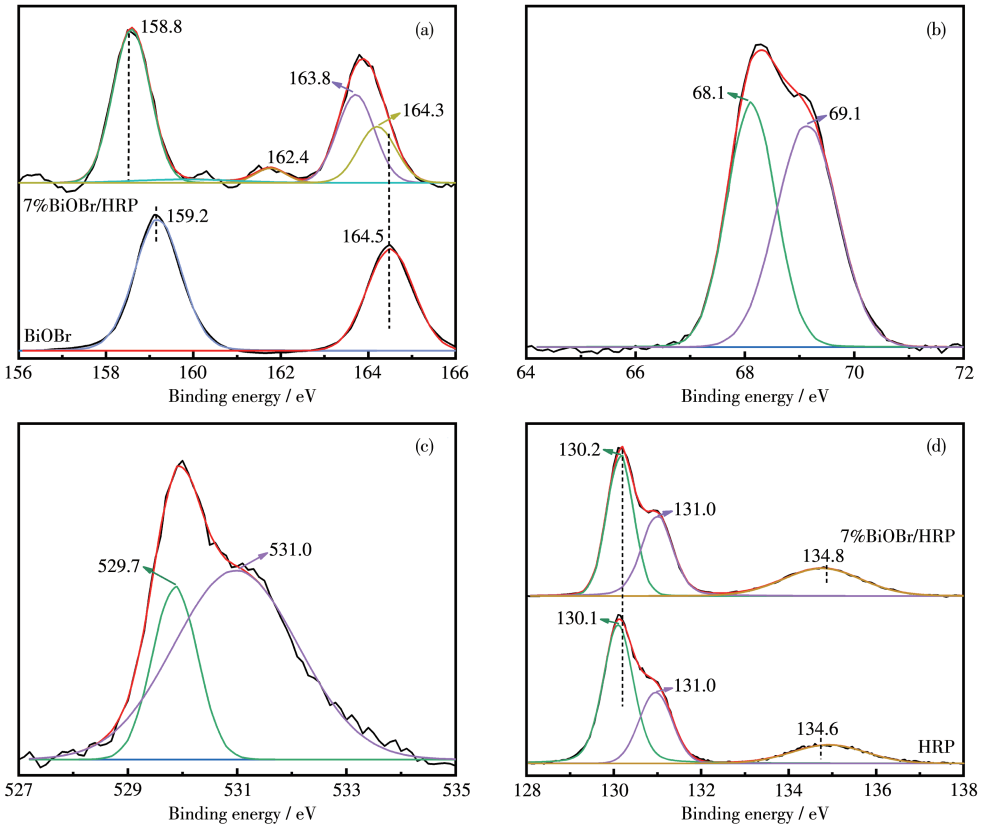

Fig.5 (a) Bi4*f*, (b) Br3*d*, (c) O1*s*, and (d) P2*p* XPS spectra of HRP, BiOBr, and 7%BiOBr/HRP

2.2 Photocatalytic tests

The photocatalytic performance of the sample was evaluated by simulating the photoreduction of Cr(Ⅵ) under visible light. From Fig. 6a, Cr(Ⅵ) was almost no

self-reduction spontaneously under visible light with the involvement of pure BiOBr, meaning the high stability of the selected model pollutant. The photoreduction ability of BiOBr/HRP composites to Cr (Ⅵ) improved compared with that of pure HRP and BiOBr. The above results showed that the granular BiOBr in the composite was uniformly dispersed on the porous HRP surface, which improved the specific surface area and porosity so that the target substance Cr(Ⅵ) could be easily adsorbed. Furthermore, the adsorption rate under dark conditions was boosted. Within a certain range, increasing the mass fraction of BiOBr may enhance the photoreduction ability of the composite to Cr(Ⅵ). The photoreduction capacity of the 7%BiOBr/HRP composite to Cr(Ⅵ) reached the maximum value, whereas the photoreduction ability of the 9%BiOBr/HRP composite was decreased. The reasons were attributed to the excess BiOBr in the composite, which reduced the contact between HRP and Cr(Ⅵ), and a large number of electrons transferred to the surface of the photocatalyst. After all, it is difficult for BiOBr to reduce Cr(Ⅵ), so the catalytic activity of the composite decreased. In addition, the excessive deposition of BiOBr on the HRP surface formed new photo-generated electron and hole pair centers, which also led to the reduction of catalytic activity. Therefore, an appropriate amount of BiOBr and HRP formed heterostructure enhanced photocatalytic performance than pure HRP or BiOBr photocatalyst, whereas excessive BiOBr lower both the light absorption capacity of the catalyst and the photoreduction ability of the composite.

The reaction results were simulated by first-order kinetics. Fig.6b was the kinetic curves of Cr(Ⅵ) photoreduction by HRP, BiOBr, and BiOBr/HRP, which accorded with the first-order kinetic model. The formula was as follows:

$$\ln(c_t/c_0')=-kt \quad (1)$$

$$t_{1/2}=\ln 2/k \quad (2)$$

where c_0' is the concentration of solution after dark adsorption equilibrium, c_t is the remaining concentration of Cr(Ⅵ) after different times of light exposure, k is the rate constant, t is the reaction time, and $t_{1/2}$ is the half-life of the composite. With the enhancement of BiOBr dosage, the k showed an increasing trend, and the increasing range first increased then decreased (Fig.6b). The k values of HRP, 5%BiOBr/HRP, 7%BiOBr/HRP, and 9%BiOBr/HRP were 0.037 6, 0.048 8, 0.188, and 0.123 min^{-1}, respectively. The photoreduction rate constant of 7%BiOBr/HRP was five times higher than that of pure HRP. In addition, the half-lives of HRP, 5%BiOBr/HRP, 7%BiOBr/HRP, and 9%BiOBr/HRP can be calculated from Eq.**2** as 18.43, 14.20, 3.69, and 5.62 min, which also reflected that the catalytic activities of the composite were all better than those of pure HRP. Among them, it is noteworthy that 7%BiOBr/HRP had the shortest photoreduction half-life. In combination with the above data, 7%BiOBr/HRP showed better photocatalytic reduction performance, which may be due to the heterostructure being more favorable to the exposure of active sites, it provided more contact opportunities for photogenerated carriers and target molecules. Meanwhile, the structure made the photocarriers of the composite catalyst have a shorter transmission distance, which helped to reduce the recombination rate of the photo-generated electron and hole pair and could improve the quantum efficiency of the

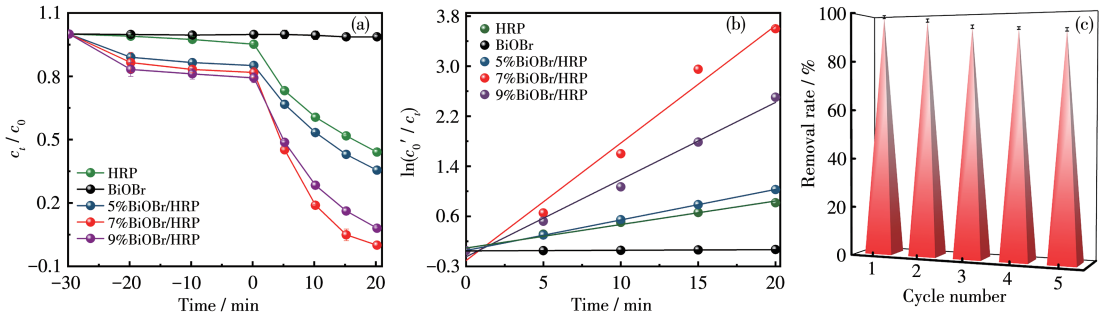

Fig.6　Photoreduction curves (a) and rate curves (b) of C(Ⅵ) over HRP, BiOBr, 5%BiOBr/HRP, 7%BiOBr/HRP, and 9%BiOBr/HRP; (c) Recycling test of 7%BiOBr/HRP for Cr((Ⅵ)

photocatalyst, thus enhancing the photocatalytic performance.

7%BiOBr/HRP after the reaction was collected to investigate the stability and reusability. Under the same conditions, repeated five times of above-mentioned photocatalytic Cr(Ⅵ) reduction experiments (Fig. 6c). The photocatalytic efficiency of the composite only decreased by 7%, which may be caused by the loss of photocatalyst in the washing process. It was demonstrated that 7%BiOBr/HRP had good stability during the photoreduction of Cr(Ⅵ) process.

2.3 Catalyst mechanism analysis

UV-Vis DRS was used to determine the light absorption characteristics of the sample. The absorption edges of pure HRP and BiOBr were 722.5 and 463.5 nm (Fig. 7a), both of which were visible light-responsive photocatalysts. While HRP had a wider light response range and higher light absorption intensity than BiOBr. For the 7%BiOBr/HRP composite, it was not only broadened the light absorption edge band (759.5 nm) but also enhanced the light absorption intensity compared to HRP and BiOBr. The forbidden bandwidth of the material was calculated by the following empirical formula[33]:

$$A=-\lg R \quad (3)$$

$$F(R)=(1-R)^2/(2R) \quad (4)$$

where R is the reflectivity and A is the absorption coefficient. Use Eq.**3** to find the different reflectance corresponding to each absorbance, then find $E=1\ 240/\lambda$ (λ is the wavelength) as the horizontal coordinate, use Eq.**4** to find $F(R)$, and then use $[F(R)E]^2$ as the vertical coordinate to get the band gap spectrum. The intercept of the tangent line on the abscissa is the band gap width. The forbidden bandwidth (E_g) values of HRP and BiOBr were 1.77 and 2.85 eV, respectively (Fig. 7b). The larger the E_g of the semiconductor, its absorption ability of visible light would be weakened. Compared with pure BiOBr, the smaller E_g value of HRP meant that when compounded it widened the absorption range of the composite and enlarged its utilization rate of visible light.

The steady-state and time-resolved PL analyzed were performed to gain further understanding of the separation and transfer efficiency of charge carriers as well as their capture behavior[34]. The obtained steady-state PL spectra of HRP, BiOBr, and 7%BiOBr/HRP

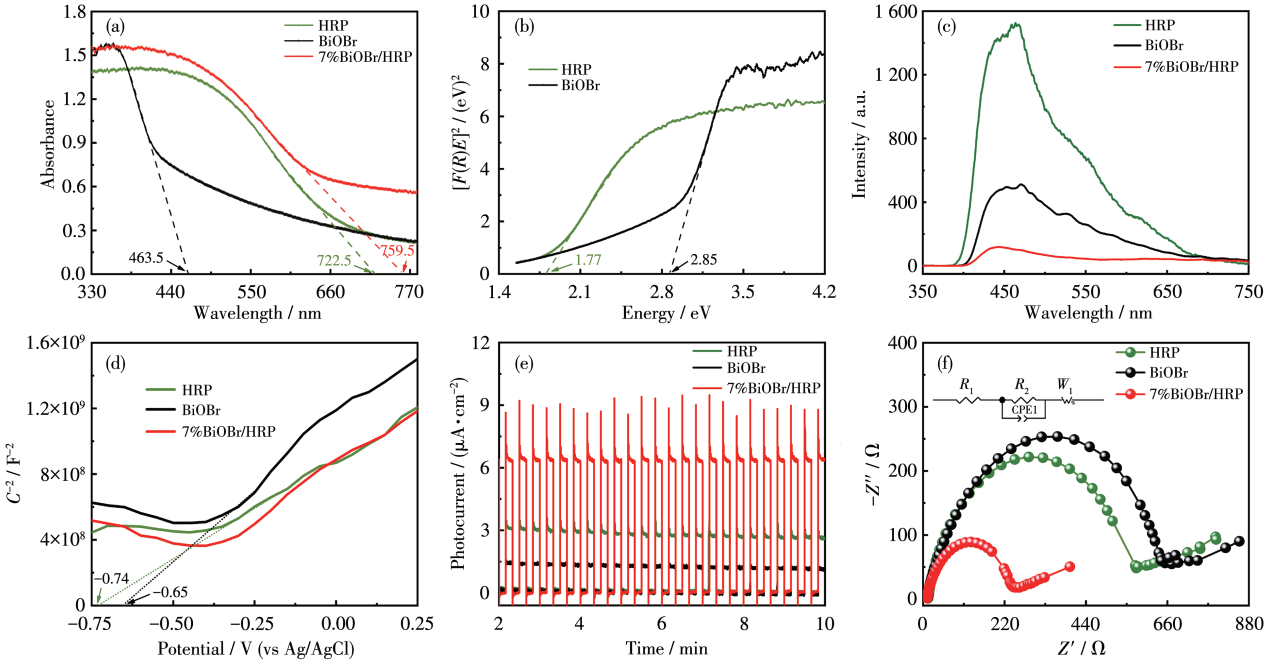

Inset: the corresponding equivalent circuit model

Fig.7 (a) UV-Vis DRS spectra and (b) band gap widths of HRP and BiOBr; (c) Photoluminescence spectra, (d) Mott-Schottky curves, (e) current-time curves, and (f) Nyquist plots of HRP, BiOBr, and 7%BiOBr/HRP

that excited at 325 nm were displayed in Fig.7c. For HRP, a strong emission peak can be observed near 440 -480 nm, which was produced by the electron-hole pair recombination. While the fluorescence intensity of BiOBr was weaker than that of HRP due to the alternated arrangement of the internal double Br^- and $[Bi_2O_2]^{2+}$ formed a laminar structure, which induced dipoles to separate electron and hole pairs efficiently. A weaker fluorescence signal meant a lower recombination rate. The PL intensity of 7%BiOBr/HRP was the weakest compared with the pure HRP and BiOBr, indicating it had the lowest recombination rate for electron - hole pairs. This demonstrated that the formation of the BiOBr/HRP heterojunction contributed to the separation of photoinduced charge carriers.

2.3.1 Mott-Schottky curve

The band structure of the sample was examined to analyze the mechanism of the above experimental results (Fig.7d). The tangent slope of all samples in the Mott-Schottky curve was positive, which indicated that the samples were n - type semiconductors. Making a tangent line to the curve, and the abscissa value of the intersection point of the curve extension line and the horizontal tangent line was the flat-band potential (E_{fb}). It can be seen directly that the corresponding values of HRP and BiOBr were −0.74 and −0.65 V (vs Ag/AgCl), respectively, and then converted to the hydrogen standard electrode potential using the following formula:

$$E_{fb\ (vs\ NHE)}=E_{fb\ (pH=0,\ vs\ Ag/AgCl)}+E_{AgCl}+0.059pH \quad (\mathbf{5})$$

E_{AgCl} is 0.197 V, and the pH of the electrolyte is 7.0. Thus, the E_{fb} values of HRP and BiOBr were −0.13 and −0.04 V (vs NHE), respectively. For n - type semiconductors, the E_{fb} was 0.1 - 0.3 V higher than the conduction band (CB) potential (E_{CB}). Therefore, the estimated CB potentials of HRP and BiOBr were −0.33 and −0.24 V (vs NHE), respectively. By combining the formula $E_g=E_{VB}-E_{CB}$, the E_{VB} (the valance band (VB) potential) of HRP and BiOBr can be 1.44 and 2.61 V (vs NHE), respectively. By the slope of the Mott-Schottky plots, the carrier density (N_d) of the prepared electrode can be determined using the formula:

$$N_d=(2/e_0\varepsilon\varepsilon_0)[d(1/C^2)/dV]^{-1} \quad (\mathbf{6})$$

where e_0 is the element charge (1.602×10^{-19} C), ε is the relative dielectric constant of the semiconductor (RP: 75 $F\cdot m^{-1}$), ε_0 is the dielectric constant of the vacuum ($8.854\ 187\ 817\times10^{-12}$ $F\cdot m^{-1}$), and $[d(1/C^2)/dV]^{-1}$ is represented the reciprocal of the slope.

The inverse of the slope was proportional to the photoanode carrier density, which meant that the smaller the slope of the curve, the higher the N_d. The 7%BiOBr/HRP composite had the lowest slope of the curve, implying that its photoanode had the highest N_d. The high N_d accelerated the migration rate of photogenerated charge carriers of the composite, which was conducive to the charge transfer between the composite and the interface solution.

2.3.2 Photocurrent and electrochemical impedance spectra

In addition to improving the optical absorption of visible light, the incorporation of BiOBr could accelerate the separation and transfer of photogenerated carriers. The transient photocurrent response and electrochemical impedance spectra were conducted to extensively study the promoted generation and transfer of photoinduced electron - hole pairs in the heterostructures. Current-time curves of HRP, BiOBr, and 7%BiOBr/HRP composite with 24 times intermittent on/off cycles under illumination (Fig.7e), which could be observed clearly that all the samples promptly generate photocurrent and remained steady after several on/off cycles. It was well established that the higher photocurrent density indicated the slower recombination rate of photogenerated carriers. The photocurrent value of 7%BiOBr/HRP was calculated to be 6.5 $\mu A\cdot cm^{-2}$, which was about two times and four times as compared with that of HRP and BiOBr, revealing better separation efficiency and prolonged lifetime of photo - generated electron and hole pairs in 7%BiOBr/HRP.

The electrochemical impedance spectra of the samples were further tested to understand the resistance of the photocarrier transport process. A smaller radius of arc meant the less resistance to carrier transport. The arc radius of BiOBr was the largest, followed by the HRP, which indicated that the resistance of photocarrier transport in HRP was grand (Fig.7f). Nonetheless, the arc radius of 7%BiOBr/HRP was the smallest,

which pinpointed that proper BiOBr combined with HRP can reduce the resistance of the photocarrier transport. On the other hand, suggesting that the heterostructures permit fast transport and separation of photoinduced charge carriers owing to the lower charge-transfer resistance. It's worth noting that R_1 and R_2 in the equivalent circuits represent the resistance between the working and reference electrodes and the resistance of the charge transfer between the electrolyte and electrode, respectively[4]. Whereas CPE was a parameter for constant phase angle element, W_1 referred to the diffusion impedance in an electrochemical reaction.

The results of the photocatalytic activity evaluation found that the photocatalytic activity of the BiOBr/HRP composites was better than that of pure HRP because the BiOBr particles were well dispersed on the surface of HRP. The close contact between the two promoted the interfacial charge transfer and significantly enhanced the interfacial activity to some extent, reducing the charge transfer resistance inside the catalyst and the recombination rate of photo-generated electron and hole pairs. Therefore, speeding up the transfer rate of photogenerated carriers could accelerate the photocatalytic reactivity for Cr(Ⅵ) removal.

Based on the above characterization results, the reaction mechanism was proposed (Fig.8). When HRP and BiOBr were in close contact, the electrons in HRP spontaneously transferred across the interface to BiOBr until they had the same Fermi level[35]. Therefore, HRP lost electrons, which had a positive charge at the interface, whereas BiOBr gained electrons and carried a negative charge at the interface. An internal electric field was formed at the interface by the transfer of HRP to BiOBr, which facilitates the transfer and separation of photogenerated carriers[36]. When the composite was exposed to visible light irradiation, HRP was more easily excited to generate electron-hole pairs. Electrons in the VB of HRP were excited by the photon and transferred to its CB, leaving a large number of holes in VB. Due to the role of the inner electric field and the formation of type-Ⅱ heterojunction between BiOBr and HRP, photogenerated electrons accumulate in the CB of BiOBr and holes accumulate in the VB of HRP, that process played a crucial role in separating photogenerated carriers and improving photocatalytic performance.

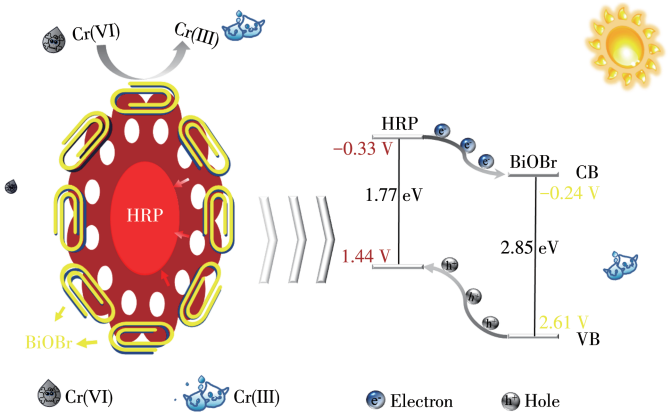

Fig.8 Photocatalytic mechanism of BiOBr/HRP

3 Conclusions

The BiOBr/HRP composite photocatalyst was assembled using the hydrothermal method. Noteworthily, a reasonable amount of BiOBr could effectively regulate the particle size of the composite, enlarged the specific surface area, increase the active sites on the surface, and promoted the diffusion and transfer of related reaction substances in the process of catalytic reaction. The 7%BiOBr/HRP composite showed good photoreduction ability to Cr(Ⅵ), 40 mg·L^{-1} solution could be thoroughly reduced in about 20 min, its rate constant was five times that of pure HRP. Based on their remarkable photocatalytic performance, BiOBr/

HRP heterostructures had great potential as efficient and stable visible-light-driven photocatalysts for water environmental purification and remediation applications.

References:

[1]Wei K X, Faraj Y, Yao G, Xie R Z, Lai B. Strategies for improving perovskite photocatalysts reactivity for organic pollutants degradation: A review on recent progress. *Chem. Eng. J.*, **2021**,**414**:128783

[2]Ansari S A, Khan Z, Ansari M O, Cho M H. Earth-abundant stable elemental semiconductor red phosphorus-based hybrids for environmental remediation and energy storage applications. *RSC Adv.*, **2016**,**6**(50):44616-44629

[3]Wu C X, Jing L, Deng J G, Liu Y X, Li S, Lv S J, Sun Y J, Zhang Q C, Dai H X. Elemental red phosphorus-based photocatalysts for environmental remediation: A review. *Chemosphere*, **2021**,**274**:129793

[4]Li S T, Wang P F, Zhao H X, Wang R D, Jing R S, Meng Z L, Li W Z, Zhang Z L, Liu Y Y, Zhang Q, Li Z. Fabrication of black phosphorus nanosheets/BiOBr visible light photocatalysts via the co-precipitation method. *Colloids Surf. A*, **2021**,**612**:125967

[5]Wang Z Z, Wang K, Li Y, Jiang L S, Zhang G K. Novel $BiSbO_4$/BiOBr nanoarchitecture with enhanced visible-light driven photocatalytic performance: Oxygen-induced pathway of activation and mechanism unveiling. *Appl. Surf. Sci.*, **2019**,**498**:143850

[6]Zhu Y K, Ren J, Zhang X L, Yang D J. Elemental red phosphorus-based materials for photocatalytic water purification and hydrogen production. *Nanoscale*, **2020**,**12**(25):13297-13310

[7]Qi L L, Dong K Y, Zeng T, Liu J Y, Fan J, Hu X Y, Jia W L, Liu E Z. Three-dimensional red phosphorus: A promising photocatalyst with excellent adsorption and reduction performance. *Catal. Today*, **2018**, **314**:42-51

[8]Guo C C, Du H, Ma Y H, Qi K Z, Zhu E Q, Su Z, Huojiaaihemaiti M, Wang X. Visible-light photocatalytic activity enhancement of red phosphorus dispersed on the exfoliated kaolin for pollutant degradation and hydrogen evolution. *J. Colloid Interface Sci.*, **2021**,**585**:167-177

[9]Yuan Y P, Cao S W, Liao Y S, Yin L S, Xue C. Red phosphor/g-C_3N_4 heterojunction with enhanced photocatalytic activities for solar fuels production. *Appl. Catal. B-Environ.*, **2013**,**140-141**:164-168

[10]Zhu Y K, Li J Z, Dong C L, Ren J, Huang Y C, Zhao D M, Cai R S, Wei D X, Yang X F, Lv C X, Theis W G, Bu Y Y, Han W, Shen S H, Yang D J. Red phosphorus decorated and doped TiO_2 nanofibers for efficient photocatalytic hydrogen evolution from pure water. *Appl. Catal. B-Environ.*, **2019**,**255**:117764

[11]Zhu E Q, Ma Y H, Du H, Qi K Z, Ainiwa M, Su Z. Three-dimensional bismuth oxide/red phosphorus heterojunction composite with enhanced photoreduction activity. *Appl. Surf. Sci.*, **2020**,**528**:146932

[12]Wang J, Pi M Y, Zhang D K, Chen S J. The visible-light photocatalytic activity for enhancing RhB degradation and hydrogen evolution from $SrTiO_3$ nanoparticles decorated red phosphorus nanorods as photocatalysts. *J. Phys. D*: *Appl. Phys.*, **2020**,**53**(8):085501

[13]Zong S K, Wei W, Cui H L, Jiang Z F, Lü X M, Zhang M, Xie J M. A novel synthesis of P/$BiPO_4$ nanocomposites with enhanced visible-light photocatalysis. *Mater. Res. Innovations*, **2015**,**19**(5):361-367

[14]Majhi D, Das K, Mishra A, Dhiman R, Mishra B G. One pot synthesis of CdS/BiOBr/$Bi_2O_2CO_3$: A novel ternary double Z-scheme heterostructure photocatalyst for efficient degradation of atrazine. *Appl. Catal. B-Environ.*, **2020**,**260**:118222

[15]Imam S S, Adnan R, Mohd Kaus N H. Immobilization of BiOBr into cellulose acetate matrix as hybrid film photocatalyst for facile and multicycle degradation of ciprofloxacin. *J. Alloy. Compd.*, **2020**,**843**: 155990

[16]Gao Z Y, Yao B H, Xu T T, Ma M M. Effect and study of reducing agent $NaBH_4$ on Bi/BiOBr/CdS photocatalyst. *Mater. Lett.*, **2020**,**259**: 126874

[17]Mao W T, Bao K Y, Cao F P, Chen B K, Liu G Y, Wang W B, Li B B. Synthesis of a $CoTiO_3$/BiOBr heterojunction composite with enhanced photocatalytic performance. *Ceram. Int.*, **2017**,**43**(3):3363-3368

[18]Ren X Z, Wu K, Qin Z G, Zhao X C, Yang H. The construction of type Ⅱ heterojunction of Bi_2WO_6/BiOBr photocatalyst with improved photocatalytic performance. *J. Alloy. Compd.*, **2019**,**788**:102-109

[19]Zhang J L, Zhang L S, Shen X F, Xu P F, Liu J S. Synthesis of BiOBr/WO_3 p-n heterojunctions with enhanced visible light photocatalytic activity. *CrystEngComm*, **2016**,**18**(21):3856-3865

[20]Bai Y, Shi X, Wang P Q, Wnag L, Zhang K, Zhou Y, Xie H Q, Wang J N, Ye L Q. $BiOBr_xI_{1-x}$/BiOBr heterostructure engineering for efficient molecular oxygen activation. *Chem. Eng. J.*, **2019**,**356**:34-42

[21]Heidari S, Haghighi M, Shabani M. Sunlight-activated BiOCl/BiOBr-$Bi_{24}O_{31}Br_{10}$ photocatalyst for the removal of pharmaceutical compounds. *J. Cleaner Prod.*, **2020**,**259**:120679

[22]Zou X J, Dong Y Y, Zhang X D, Cui Y B, Ou X X, Qi X H. The highly enhanced visible light photocatalytic degradation of gaseous *o*-dichlorobenzene through fabricating like-flowers $BiPO_4$/BiOBr p-n heterojunction composites. *Appl. Surf. Sci.*, **2017**,**391**:525-534

[23]Kim S R, Jo W K. Boosted photocatalytic decomposition of nocuous organic gases over tricomposites of N-doped carbon quantum dots, $ZnFe_2O_4$, and BiOBr with different junctions. *J. Hazard. Mater.*, **2019**,**380**:120866

[24]Cao Q W, Cui X, Zheng Y F, Song X C. A novel $CdWO_4$/BiOBr p-n heterojunction as visible light photocatalyst. *J. Alloy. Compd.*, **2016**, **670**:12-17

[25]Fu S, Yuan W, Liu X M, Yan Y H, Liu H P, Li L, Zhao F Y, Zhou J G. A novel 0D/2D WS_2/BiOBr heterostructure with rich oxygen vacancies for enhanced broad-spectrum photocatalytic performance. *J. Colloid Interface Sci.*, **2020**,**569**:150-163

[26]Guo Y X, Huang H W, He Y, Tian N, Zhang T R, Chu P K, An Q, Zhang Y H. In situ crystallization for fabrication of a core-satellite structured BiOBr-CdS heterostructure with excellent visible-light-responsive photoreactivity. *Nanoscale*, **2015**,**7**(27):11702-11711

[27]Han A J, Zhang H W, Lu D, Sun J L, Chuah G K, Jaenicke S. Efficient photodegradation of chlorophenols by BiOBr/$NaBiO_3$ heterojunctioned composites under visible light. *J. Hazard. Mater.*, **2018**, **341**:83-92

[28]Hu T P, Yang Y, Dai K, Zhang J F, Liang C H. A novel Z-scheme Bi_2MoO_6/BiOBr photocatalyst for enhanced photocatalytic activity under visible light irradiation. *Appl. Surf. Sci.*, **2018**,**456**:473-481

[29]Zhu E Q, Zhao S X, Du H, Ma Y H, Qi K Z, Guo C C, Su Z, Wang X, Wu Z D, Wang Z H. Construction of $Bi_2Fe_4O_9$/red phosphorus heterojunction for rapid and efficient photo-reduction of Cr(Ⅵ). *J. Am. Ceram. Soc.*, **202**1,**104**(10):5411-5423

[30]Chen X, Zhang X, Li Y H, Qi M Y, Li J Y, Tang Z R, Zhou Z, Xu Y J. Transition metal doping BiOBr nanosheets with oxygen vacancy and exposed {102} facets for visible light nitrogen fixation. *Appl. Catal. B-Environ.*, **2021**,**281**:119516

[31]Kannan V, Arredondo M, Johann F, Hesse D, Labrugere C, Maglione M, Vrejoiu I. Strain dependent microstructural modifications of $BiCrO_3$ epitaxial thin films. *Thin Solid Films*, **2013**,**545**:130-139

[32]Gao M C, Zhang D F, Pu X P, Li H, Lv D D, Zhang B B, Shao X. Facile hydrothermal synthesis of Bi/BiOBr composites with enhanced visible-light photocatalytic activities for the degradation of rhodamine B. *Sep. Purif. Technol.*, **2015**,**154**:211-216

[33]Basaleh A, Ismail A A, Mohamed R M. Novel visible light heterojunction CdS/Gd_2O_3 nanocomposites photocatalysts for Cr(Ⅵ) photoreduction. *J. Alloy. Compd.*, **2022**,**927**:166988

[34]Bao Y C, Chen K Z. Novel Z-scheme BiOBr/reduced graphene oxide/protonated g-C_3N_4 photocatalyst: Synthesis, characterization, visible light photocatalytic activity and mechanism. *Appl. Surf. Sci.*, **201**8, **437**:51-61

[35]陈永胜, 郑健飞, 朱思龙, 熊梦杨, 聂龙辉. BiOBr/$BiPO_4$ p-n异质结光催化剂的一步水热法制备及性能. 无机化学学报, **2021**,**37**(10):1828-1838

CHEN Y S, ZHENG J F, ZHU S L, XIONG M Y, NIE L H. One-step hydrothermal preparation and performance of BiOBr/$BiPO_4$ p-n heterojunction photocatalyst. *Chinese J. Inorg. Chem.*, **2021**,**37**(10):1828-1838

[36]An W J, Cui W Q, Liang Y H, Hu J S, Liu L. Surface decoration of $BiPO_4$ with BiOBr nanoflakes to build heterostructure photocatalysts with enhanced photocatalytic activity. *Appl. Surf. Sci.*, **2015**, **351**:1131-1139